EUROPEAN FUSION DEVELOPMENT AGREEMENT

EFDA–JET–PR(05)03

T. Onjun, A. H Kritz, G. Bateman, V. Parail, and JET EFDA contributors

# MHD-Calibrated ELM Model in Simulations of ITER

# MHD-Calibrated ELM Model in Simulations of ITER

T. Onjun[1], A. H Kritz[2], G. Bateman[2], V. Parail[3] and JET EFDA contributors*

[1]*Sirindhorn International Institute of Technology, Klong Luang, Pathumthani 12121, Thailand*
[2]*Lehigh University Physics Department, 16 Memorial Drive East, Bethlehem, PA 18015, USA*
[3]*EURATOM/UKAEA Fusion Association, Culham Science Centre, Abingdon, Oxon, OX14 3DB, UK*
** See annex of J. Pamela et al, "Overview of JET Results ",*
*(Proc.20 th IAEA Fusion Energy Conference, Vilamoura, Portugal (2004).*

Preprint of Paper to be submitted for publication in
Physics of Plasmas

“This document is intended for publication in the open literature. It is made available on the understanding that it may not be further circulated and extracts or references may not be published prior to publication of the original when applicable, or without the consent of the Publications Officer, EFDA, Culham Science Centre, Abingdon, Oxon, OX14 3DB, UK.”

“Enquiries about Copyright and reproduction should be addressed to the Publications Officer, EFDA, Culham Science Centre, Abingdon, Oxon, OX14 3DB, UK.”

## 1. INTRODUCTION

High confinement mode (H-mode) discharges in tokamaks provide good energy confinement and have acceptable particle transport rates for impurity control. Because of these properties, H-mode is one of the scenarios that will be used in burning plasma experiments such as the International Thermonuclear Experimental Reactor (ITER) [1]. However, H-mode discharges are often perturbed by quasi-periodic bursts of MHD activity at the edge of the plasma, which are known as edge localized modes (ELMs). Each ELM crash results in a rapid loss of particles and energy from the edge of the plasma, which can reduce the average global energy content by 10-20% [2]. Furthermore, these transient bursts of energy and particles into the scrape-off layer produce high peak heat loads on the divertor plates. On the other hand, the ELMs remove heat and particles, including impurities, from the region near the separatrix. ELMs also play an essential role in the control of the pedestal height in H-modes, and it has been shown both in experiments and in simulations that the parameters at the top of the pedestal have a strong influence on the performance of H-mode discharges [3, 4, 5, 6]. Consequently, the production of fusion power in ITER is expected to depend sensitively on the behavior of ELMs.

In recent ITER studies, simulations have been carried out to predict the performance of ITER using several integrated modeling codes, such as BALDUR [7], XPTOR [8], and ASTRA [9]. The BALDUR simulations for ITER were carried out from the center of the plasma to the top of the pedestal without including the effect of ELM crashes [10]. The temperature at the top of the pedestal, $T_{\rm ped}$, is one of the boundary conditions required in BALDUR H-mode simulations. In Ref. [10], $T_{\rm ped}$ was calculated using a simple pedestal temperature model in which the pressure gradient is limited by the first ballooning stability and the pedestal width is based on magnetic shear and flow shear stabilization [11]. A similar treatment for the boundary conditions is used in the ITER simulations with the XPTOR code [5]. The simulations of ITER carried out using the BALDUR code and the XPTOR code do not include the effect of ELMs. Somewhat more advanced simulations of ITER have been carried using the ASTRA code [12]. In these simulations, the pedestal is produced by ExB shear and magnetic shear stabilization, and a simple model of ELMs, based on the pressure-driven ballooning mode, is employed to simulate the effect of ELMs in a time-averaged fashion. However, the ELM model that was used did not include triggering of ELMs resulting from current-driven peeling modes. Simulations carried out using the ASTRA code yielded, for JET and ASDEX-Upgrade ELMy H-mode discharges, temperature profiles similar to the experimental profiles, and, for ITER, values of fusion $Q$ in the range 12 to 16.

In this paper, self-consistent simulations of the standard H-mode ITER scenario are carried out using the JETTO modeling code [13] in which theory motivated models are used for the H-mode pedestal and for the stability conditions that lead to the ELM crashes. Transport is described by combining the anomalous Mixed Bohm/gyro-Bohm model [14] with the NCLASS neoclassical transport model [15]. In the pedestal region, which is assumed to extend 6 cm inside the separatrix in the baseline case, the anomalous transport is completely suppressed and, consequently, the

neoclassical transport dominates. The reduction of transport within the pedestal region results in a steep pressure gradient at the edge of the plasma, which, in turn, produces a large bootstrap current density in the pedestal. The steep edge pressure gradient and large edge bootstrap current can trigger either an unstable pressure driven ballooning mode or an unstable current driven peeling mode, resulting in an ELM crash. In the simulations, an ELM crash is triggered by a pressure-driven ballooning mode if, anywhere within the pedestal region, the pressure gradient exceeds the ballooning mode stability limit, or an ELM crash is triggered by a current-driven peeling mode if the edge current density exceeds the critical edge current density of the peeling condition. These stability conditions are included in the JETTO code. The equilibrium and MHD stability analyses codes, HELENA and MISHKA [16], are then used to evaluate the edge stability of the plasma just before an ELM crash in order to calibrate and confirm the validity of the stability criteria that are used to trigger ELMs in the JETTO simulations. The stability analyses include infinite-$n$ ideal ballooning modes, finite-$n$ ballooning modes, and low-$n$ kink/peeling modes.

H-mode simulations of JET discharges, using the same transport modeling and the combination of pressure-driven ballooning modes and current-driven peeling modes to trigger ELM crashes described above, have been carried out for a number of standard H-mode scenarios. The scans include a triangularity scan [17], a power scan [18], and a gas puffing scan [19]. The simulations yielded temperature profiles that were in reasonable agreement with experimental data and resulted in a better understanding of pedestal and ELMs in H-mode plasmas [20, 21].

This paper is organized as follows. The transport code, JETTO, and equilibrium and stability codes, HELENA and MISHKA, are briefly described in Section 2. ITER simulation results and the associated stability analyses are presented in Section 3. The dependence of the value of fusion $Q$ on the assumed width of the pedestal and on the heating power is examined in Section 4 and the test of self-sustain heating is carried out in Section 5. The conclusions are contained in Section 6.

## 2. MODELING CODES

In this paper, simulations of an ITER scenario are carried out using the predictive JETTO code and MHD stability analyses are carried out using the HELENA and MISHKA codes. These codes are described in this section.

### *2.1. THE JETTO CODE*

The $1\frac{1}{2}$D JETTO transport code is used to evolve the plasma current, temperatures and density profiles throughout the plasma, including both the core and pedestal regions. The core transport is calculated using the Mixed Bohm/gyro-Bohm model [14] together with the NCLASS neoclassical model [15]. For the pedestal region, two assumptions are applied in this paper. One assumption is that of the pedestal width is fixed equal to 6 cm. (This assumption is relaxed in Section 4 in order to examine the dependence of the simulation results on pedestal width.) The second assumption is that the anomalous turbulent transport is completely suppressed in the region between the top of the

pedestal and the separatrix resulting in the establishment of a steep gradient region. In the pedestal region prior to an ELM crash, transport is computed by taking all the diagonal elements of the transport matrix within the pedestal equal to the ion neoclassical thermal conductivity, calculated at the top of the pedestal using NCLASS [15]. The use of constant ion neoclassical diffusion in the pedestal region is based on the consideration that since the pedestal width is usually of the order of the ion orbit width (or banana width), there is limited variation in the neoclassical transport across the barrier. The boundary conditions for the electron and ion temperatures and for the ion density are imposed at the separatrix in the simulations. The electron and ion temperatures at the separatrix are taken to be 20 eV, and the deuterium and tritium densities at the separatrix are assumed to be $3.5 \times 10^{19}$ m$^{-3}$. It is found that the values used for the electron and ion temperature at the separatrix influence the time evolution of the ELMs, but do not affect the overall confinement [17], particularly since strong gas puffing was not used citelonn04b.

In the JETTO simulations, the reduced transport within the pedestal region results in the development of a steep pressure gradient, which causes an increase in the bootstrap current within the pedestal. The increase of edge pressure gradient, and the associated increase in the edge current density, leads to a destabilization of either a pressure-driven ballooning mode [23, 24] or a current-driven peeling mode [25, 26, 27, 28]. The resulting MHD instability triggers an ELM crash, which causes a loss of plasma energy and particles to the wall.

The criterion used in the JETTO simulation for an ELM crash triggered by a pressure-driven ballooning mode is that the normalized pressure gradient, $\alpha$, anywhere within the pedestal exceeds the critical value of the normalized pressure gradient, $\alpha_c$:

$$\alpha \equiv -\frac{2\mu_0 q^2}{B_T^2}\frac{R}{a}\frac{\partial p}{\partial \rho} > \alpha_c. \tag{1}$$

where $\alpha_c$ is a prescribed number that is calibrated employing the stability analyses carried out using the HELENA and MISHKA codes. Note that the notation and units used in this paper are described in Table 1. The criterion for an ELM crash triggered by a current-driven peeling mode is that the edge current density exceeds a critical current density. This criterion is evaluated for the width of 1 cm from the separatrix. This critical current density model is based on an analytical expression developed in Ref. [26]. For axisymmetric toroidal geometry, the current-driven peeling instability condition is

$$\sqrt{1-4D_M} + C_{\text{vac}} < 1 + \frac{1}{\pi q'}\oint \frac{\mu_0 j_\parallel B_T}{R^2 B_p^3} dl \tag{2}$$

where $D_M$ is the Mercier coefficient, which is proportional to pressure gradient; $C_{\text{vac}}$ is a parameter related to the vacuum energy, which is taken to be 0.2 for the baseline simulations in this study; $q'$ is the derivative of the safety factor with respect to the poloidal flux; $j_\parallel$ is the current density parallel to the magnetic field $\mathbf{B}$; $R$ is the major radius; $B_p$ is the poloidal magnetic field; and $dl$ is the poloidal arc length element for the integral around a flux surface.

When the condition for an ELM crash is satisfied in the JETTO simulation, either by the

pressure-driven ballooning mode criterion (Eq. 1) or by the current-driven peeling mode criterion (Eq. 2), an ELM crash is produced by significantly increasing the diagonal coefficients for electron and ion thermal transport within the pedestal region. The increased levels of transport are maintained for a time interval $\tau_{\rm ELM} = 0.5$ ms. A wide range of H-mode simulations have been carried out using this ELM crash treatment, and it has been demonstrated that these simulations reproduce the plasma profiles in the corresponding JET discharges [17, 18, 19].

### *2.2. MHD STABILITY CODES*

In this paper, MHD stability analyses are carried out using the HELENA and MISHKA codes [16]. The HELENA code is employed to compute the stability of infinite-$n$ ideal ballooning modes and, based on the plasma profiles and equilibrium information generated by JETTO code, produces an equilibrium with the higher resolution that is needed for the MISHKA code analyses. MISHKA is then applied to evaluate the stability criteria for finite-$n$ ballooning and low-$n$ kink (peeling) modes. In this study, the stability analysis carried out with the MISKHA code is for modes with toroidal mode number $n = 1$ to $n = 14$. Note that the version of the MISHKA code used in this paper is based on the ideal MHD model.

## 3. SIMULATION RESULTS AND DISCUSSION

### *3.1. BASELINE SIMULATION*

The ITER simulation is carried out for the baseline parameters shown in Table 2 using the JETTO code. The core transport is calculated using the Mixed Bohm/gyro-Bohm transport model [14] for the anomalous transport and the NCLASS model [15] for the neoclassical transport. The effect of sawtooth oscillations, which periodically reduce the central plasma profiles, is also included. For simplicity, it is assumed that the mixing radius of each sawtooth oscillation extends from the plasma center up to $q = \sqrt{2}$ radius and that each sawtooth crash occurs every 10.0 s. The pedestal width, $\Delta$, is assumed to be equal to 6 cm in the baseline simulations. There are a number of pedestal width scalings proposed in the literature, such as $\Delta \propto \rho_i s^2$ [11, 17, 29], $\Delta \propto R\sqrt{\beta_\theta}$ [11, 30] and $\Delta \propto \sqrt{\rho_i R q}$ [11], where $\rho_i$ is the ion gyro-radius, $s$ is magnetic shear, $\beta_\theta$ is the normalized poloidal pressure, $R$ is the major radius, and $q$ is the safety factor. For $\Delta \propto \rho_i s^2$, the ITER pedestal width is approximately 5.0 cm; for $\Delta \propto R\sqrt{\beta_\theta}$, the pedestal width is approximately 6.0 cm; and for $\Delta \propto \sqrt{\rho_i R q}$, the width is approximately 4.7 cm. In Section 4, the value of the pedestal width is varied to study the sensitivity of the predicted fusion power as a function of this parameter. It is assumed that the effective charge, $Z_{\rm eff}$, is 1.4, which results from only carbon impurity, and that the input power is equal to 40 MW. The sensitivity of the performance of ITER to the level of input power is examined in Section 4. The radiation profile is taken to be the same as in the JET discharge 52009. The ITER simulations are carried out for discharges with a 50:50 mixing of deuterium and tritium.

Figure 1 shows the ion and electron temperature and electron density profiles at a time just prior to an ELM crash. It can be seen that the central electron temperature is about 33.3 keV while the central ion temperature is about 21.0 keV. The central electron temperature is higher than the central ion temperature due to the alpha heating power produced by the fusion reactions. The central ion and electron temperatures obtained in the ITER simulation carried out using the JETTO code are higher than those obtained in the corresponding simulation carried out using the BALDUR code Ref. [10]. The differences in the values of the central temperatures in the JETTO and BALDUR simulations are due, in part, to differences in the values of the temperatures at the top of the pedestal. In the JETTO simulations, the ion and electron pedestal temperatures prior to an ELM crash are approximately 4.9 keV and 4.4 keV, respectively, while in the BALDUR simulations the corresponding pedestal temperatures are 2.7 keV Ref. [10]. The temperature profiles in the type I ELMy H-mode plasma depend on the temperatures at the top of the pedestal [3, 4]. The pedestal temperature model used in the BALDUR code was derived based on the assumption that the pedestal pressure gradient is limited by the first ballooning mode instability limit. In this study, however, it is found that the ITER plasma obtains access to the ballooning mode second stability region, which results in a higher edge pressure gradient and, consequently, a higher pedestal temperature. Another difference between the JETTO simulations described in this paper and those carried out previously with the BALDUR code is that that the Mixed Bohm/gyro-Bohm core transport model is used in the JETTO simulations while the Multi-Mode (MMM95) core transport model was used in the BALDUR simulations in Ref. [10]. In addition to the ITER temperature profiles, the simulated density profile is shown in Fig. 1 at a time just prior to an ELM crash. It can be seen than the density profile is relatively flat, which is similar to the density profile obtained in the ITER BALDUR simulations Ref. [10]. Although the neoclassical transport model includes a particle pinch (the Ware pinch) the anomalous Mixed Bohm/gyro-Bohm transport model does not.

In the simulation shown in Fig. 1, the anamolous transport is calculated using the Mixed Bohm/gyro-Bohm transport model. The Mixed Bohm/gyro-Bohm transport model has two components; the Bohm term (which is proportional to gyro-radius) and the gyro-Bohm term (which is proportional to gyro-radius squared). The details of this transport model can be found in Ref. [14]. It is found in this simulation that the gyro-Bohm term dominates over much of the plasma. This result is opposite to the previous H-mode study using the Mixed Bohm/gyro-Bohm carried out by D. Hannum [31]. In that work, simulations were carried for 22 JET and DIII-D H-mode discharges obtained from the International Profiles Database [32]. In those simulations, the transport was dominated by the non-local Bohm term, in which the transport throughout the plasma is proportional to a finite difference approximation to the edge temperature gradient. Hence, in those simulations, the core transport depended somewhat sensitively on the value of the pedestal temperature, $T_{\rm ped}$. In the ITER simulations reported here, the transport across most of the plasma is dominated by the gyro-Bohm term, which, in the mixed Bohm/gyro-Bohm model, depends only on local plasma parameters and is not very sensitive to the temperature gradient. As a result, the

core transport model used in this paper is only moderately sensitive to the value of $T_{\rm ped}$. This will lead to an explanation given in the next section for the insensitivity of the fusion $Q$ as a function of the value of $T_{\rm ped}$.

Fig. 2 shows the plasma current density and bootstrap current density for outer half of the plasma (from $\rho = 0.5$ to $\rho = 1.0$) at a time just prior to an ELM crash. It can been seen that the current density is peaked at the edge of the plasma, which is a consequence of the bootstrap current density. Because of the large edge current density, the magnetic shear decreases to a relatively low value within the pedestal, which can lead to a possible access to the second stability region of ballooning modes. It is interesting to note that the bootstrap current density within the pedestal is larger than the total plasma current density within the pedestal. This effect is caused by the back EMF, which prevents the fast growth of the plasma current density within the pedestal, while the bootstrap current can grow rapidly as a consequence of the pressure gradient. This effect has been observed and explained in a previous study using the JETTO code [18].

The effects of ELM crashes are included in the JETTO simulations presented in this paper. An ELM crash can be triggered either by a pressure-driven ballooning mode or by a current-driven peeling mode. The effects of ELM crashes on the plasma stored energy and temperature are shown in Fig. 3. It is found that approximately 10% of stored energy at the time just before an ELM crash (45 MJ) is lost during each ELM crash. Note, the approximately 30% drop in central temperature at 20 sec. in the middle panel of Fig. 3 is the result of a sawtooth crash, not an ELM crash.

There are two types of the auxiliary heating used in the ITER simulation. The total amount of NBI heating power, $P_{\rm NBI}$, is 33 MW. The NBI heating profiles are calculated using the Pencil module with a 1 MeV negative ion beam. The NBI heating profiles for electrons and ions are shown in Fig. 4. Another source of auxiliary heating is the RF heating, $P_{\rm RF}$. The total amount of RF heating power is 7 MW. The RF heating profiles are taken from the JET high performance discharge 52009 although it is recognized that the physics of RF heating might be different in the ITER plasma. Note that Ohmic heating is small compared to other types of heating. The alpha heating power, $P_\alpha$, is also shown in Fig. 4. It can be seen that the alpha heating power, which is about 133 MW power, dominates over other types of heating and the alpha heating power is peaked at the center of the plasma. With this amount of alpha heating power, the fusion $Q$, defined as $Q \equiv 5P_\alpha/(P_{\rm NBI} + P_{\rm RF})$, is about 16.6.

### *3.2. STABILITY ANALYSIS*

In order to check the validity of the analytical ballooning stability criterion used in the JETTO code, the results of the JETTO simulations are linked with the HELENA and MISHKA MHD stability analysis codes. The HELENA code takes as input the self-consistent equilibrium produced by the JETTO code, that is the pressure gradient and the current density profiles, together with the corresponding magnetic configuration, at a time just before an ELM crash occurs. The HELENA code then refines the equilibrium in order to provide the resolution required for the stability anal-

ysis. The refined equilibrium is used in the HELENA code to generate a ballooning stability s-$\alpha$ diagram, and is used in the MISHKA code, to evaluate the stability criteria for finite-$n$ ballooning and low-$n$ kink/peeling modes. In this study, the stability analysis is carried out in MISHKA for toroidal mode numbers in the range of $n = 1$ to $n = 14$. Note, the version of the MISHKA code employed in this paper is based on the ideal MHD model without dissipation or flow shear.

A stability analysis is carried out using the HELENA and MISHKA codes to evaluate the edge stability at the time just before an ELM crash. Fig. 5 shows the stability s-$\alpha$ diagram for the baseline ITER simulation. In the figure, the stability s-$\alpha$ diagram is plotted for four flux surfaces within the pedestal at $\rho = 0.95, 0.96, 0.97,$ and 0.98. The circle symbol in each panel represents the location of the operational point for the pressure gradient and magnetic shear at that flux surface. The region of instability associated with the infinite-$n$ ideal ballooning modes is indicated with crosses, while the numbers indicate the most unstable mode of finite-$n$ ballooning and low-$n$ kink/peeling modes at each location on the s-$\alpha$ plane.

It can be seen in Fig. 5 that there is a wide access to the second stability region of ballooning modes. Note that the operational point at each flux surface, indicated by the circle symbol, is located at a value of alpha, the normalized pressure gradient, which is significantly higher than the peak value of alpha allowed by the first stability limit. The edge pressure gradient appears to be limited by an $n = 14$ toroidal mode. The access to second stability is probably a result of the strong shaping of the ITER plasma, particularly the fact that the ITER plasma is designed to have a triangularity of 0.48 at the separatrix. In the present-day experiments, evidence of access to second stability in high triangularity discharges has been observed in a number of tokamaks, for example DIII-D [33, 34, 35], JET [36], JT-60U [35, 37, 38] and Alcator C-Mod [39].

## 4. SENSITIVITY STUDIES

### *4.1. VARIATION OF HEATING POWER*

In Ref. [1], the scaling of the heating power required for the transition from L-mode to H-mode, $P_{L-H}$, is expressed as

$$P_{L-H}[MW] = 2.84 A_H^{-1} B_T^{0.82} \bar{n}_{20}^{0.58} R^{1.00} a^{0.81} \tag{3}$$

where $\bar{n}_{20}$ is the line average density in the unit of $10^{20}$ particles/m$^3$. Based on Eq. 3, the L-H transition power required for ITER is about 48 MW. In the simulations shown in Fig. 1, it is found that with the levels of 33 MW NBI heating power, $P_{\rm NBI}$, and 7 MW RF heating power, $P_{\rm RF}$, the total heating power, including the alpha heating power ($P_\alpha + P_{\rm NBI} + P_{\rm RF}$), is about 173 MW, which is well above the heating power needed to make the transition from L-mode to H-mode ($P_{\rm L\rightarrow H}$).

The simulations of ITER are carried with the auxiliary heating power varied. The level of the total auxiliary heating power is varied from 20 MW to 50 MW by increasing the NBI heating power from 13 MW to 43 MW and keeping the RF heating fixed at 7 MW. It is found that with a total auxillary heating power of 20 MW (13 MW of NBI and 7 MW of RF), the ion temperature

at the top of the pedestal is about several hundred electron volts. This plasma is likely to be in L-mode, rather than H-mode. The results of simulations with a total auxillary heating power of 30 to 50 MW are shown in Fig. 6, where the average pedestal temperature and average fusion $Q$ at a time just before an ELM crash are indicated for three values of the auxiliary heating power ($P_{\rm NBI} + P_{\rm RF}$). The Ohmic heating power is omitted since it is small compared to the auxiliary heating power. It can be seen in Fig.6 that as the auxiliary heating power increases, the pedestal temperature remains almost constant. The constancy of pedestal temperature with heating power is not surprising since each sequence of ELM crashes in these simulations is initially triggered by a ballooning mode and the ballooning mode criterion in Eq. 1 is independent of heating power. Consequently, the pressure gradient before an ELM crash is the same in simulations with different levels of auxiliary heating power. With a fixed pedestal width, this results in a pedestal with a relatively constant pedestal temperature prior to each ELM crash. It is found in these simulations that the central ion temperature is nearly constant at 21 keV.

### *4.2. VARIATION OF PEDESTAL WIDTH*

If the core transport model is stiff, the core profiles and fusion performance, $Q$, depend on values of temperature and pressure at the top of the pedestal. One parameter that controls the height of the pedestal is the width of the pedestal. The scaling of the pedestal width is still unclear. Previous experimental studies of pedestal scalings have found a range of results for the pedestal width in various tokamaks [11]. Some studies have found a scaling consistent with a pedestal width that is linearly proportional to the gyro-radius [40, 41, 42, 43, 44]. Earlier JET results indicated a weaker scaling for the inferred pedestal width — with the pedestal width, $\Delta$, scaling as $\Delta \propto R(\rho_\theta/R)^\nu$, where $\nu$ is in the range of $1/2$ to $2/3$ [45], $R$ is the plasma major radius and $\rho_\theta$ is the poloidal ion gyro-radius. Some early studies from DIII-D indicated that it was hard to distinguish between $\Delta/R \propto (\rho_\theta/R)^{2/3}$ and $\Delta/R \propto \beta_\theta^{1/2}$ (where $\beta_\theta$ is the plasma pressure normalized by the poloidal magnetic pressure), but later experiments with a pumped divertor were able to reduce the correlation between density and plasma current, and they supported a pedestal width scaling $\Delta/R \propto \beta_\theta^{1/2}$ [30]. It is found that the pedestal width scalings in Ref. [11] yield a pedestal width in ITER in the range of 4.7 to 6.0 cm (5.0 cm with $\Delta \propto \rho_i s^2$, 6.0 cm with $\Delta \propto R\sqrt{\beta_\theta}$, and 4.7 cm with $\Delta \propto \sqrt{\rho_i R q}$).

Simulations of ITER are carried out using the Mixed-Bohm/gyro-Bohm anomalous transport model in the JETTO code in which the value of the pedestal width is varied from 1 cm to 8 cm. In this scan, the NBI heating power and RF heating are held fixed at 33 MW and 7 MW, respectively. In Fig. 7, results from these simulations are shown with solid lines for the average pedestal temperature and the fusion $Q$ at the time just before an ELM crash, plotted as function of the pedestal width. It can be seen that the pedestal temperature and the fusion $Q$ both increase significantly as the pedestal width increases. The dashed line in the bottom panel in Fig. 7 shows the fusion $Q$ that is predicted using the Multi-Mode anomalous transport model in the BALDUR

code [10]. In the BALDUR simulations, the temperature at the top of the pedestal is used as the boundary condition at the edge of the plasma, and ELM crashes are not simulated. It is assumed that the temperature at the top of the pedestal, which is shown in the top panel of Fig. 7, is almost independent of the anomalous transport model that is used in the plasma core, since the time evolution of $T_{\rm ped}$ in the model used here depends only on the width of the pedestal, the neoclassical transport at the top of the pedestal, and the MHD instability condition that triggers each ELM crash.

## 5. TEST OF SELF-SUSTAINING HEATING

It is useful to study the issue of self-sustained heating (ignition) in ITER. Does the ITER discharge continue to produce a large amount of fusion power after the auxiliary heating power is turned off? The JETTO code is used to carry out simulations with the 40 MW auxiliary heating power turned off at 30 sec. In this simulation, the pedestal width is held fixed at 6 cm. The time history of NBI, RF and alpha power (top panel), thermal energy (middle panel), and central and pedestal temperature (bottom panel) are shown in Fig. 8. It can be seen that after the auxiliary heating is turned off, the central temperature decreases only slightly, which results in a small reduction in the alpha power. On the other hand, the ion pedestal temperature remains almost constant while the ELM frequency decreases by more than a factor of two. The fusion reactions are sustained at a level of about 100 MW of alpha power.

Figure 9 shows the ion and electron temperature profiles at a time just prior to an ELM crash before and after the auxiliary power is turned off. It can be seen that the central ion and electron temperatures at a time after the auxiliary heating is turned off are only slightly lower than that before the auxiliary heating is turned off. The electron and ion pedestal temperatures remain almost the same.

A stability analysis is carried out using the HELENA and MISHKA codes to evaluate the edge stability at a time just before an ELM crash for the ITER simulation after the auxiliary heating power turned off. In Fig. 10, the stability s-$\alpha$ diagram is plotted for the $\rho = 0.95, 0.96, 0.97,$ and 0.98 flux surfaces within the pedestal. It can be seen that the plasma still has access to the second stability region of ballooning modes, which is similar to the result before turning off the auxiliary heating power. The edge pressure gradient appears to be limited by an $n = 14$ toroidal mode.

## 6. CONCLUSION

Self-consistent simulations of ITER have been carried out using the JETTO integrated modeling code in which theory motivated models are used for the H-mode pedestal and for the stability conditions that lead to the ELM crashes. In these simulations, ELM crashes appear as a sequence of ELM crashes, in which the first ELM crash is triggered by a pressure-driven ballooning mode and the rest are triggered by a current-driven peeling mode. It is found that the baseline simulation of the ITER design yields a fusion Q of 16.6 with the pedestal height about 5 keV. The high value of the pedestal temperature results from access to the second stability of ballooning mode. The

fusion $Q$ decreases as the auxiliary heating power increases. Also, the fusion $Q$ decreases as the width of the pedestal decreases. It is found in the simulations that the ITER plasma can sustain alpha power production and access to the second stability of ballooning modes after the auxiliary heating power is shut down.

## 7. ACKNOWLEDGMENTS

One author (T. Onjun) thanks the Royal Thai Government and the Development and Promotion for Science and Technology Talents Project of Thailand (DPST) for their support. This work was conducted partly under European Fusion Development Agreement. It was supported in part by the U.S. Department of Energy (DOE) under contract No. DE-FG02-92-ER-5414 and by the UK Department of Trade and Industry and by EURATOM.

## REFERENCES


[1] R. Aymar, P. Barabaschi, and Y. Shimomura, Plasma Phys. Control. Fusion **44**, 519 (2002).

[2] J. W. Connor, Plasma Phys. Control. Fusion **40**, 191 (1998).

[3] W. Suttrop, M. Kaufmann, H. J. de Blank, *et al.*, Plasma Physics and Controlled Fusion **39**, 2051 (1997).

[4] M. Greenwald, R. L. Boivin, F. Bombarda, *et al.*, Nucl. Fusion **37**, 793 (1997).

[5] J. Kinsey, T. Onjun, G. Bateman, A. H. Kritz, A. Pankin, G. M. Staebler, and R. E. Waltz, Nucl. Fusion **43**, 1845 (2003).

[6] V. Mukhovatov, A. P. Y. Shimomura, *et al.*, Nucl. Fusion **43**, 942 (2003).

[7] C. E. Singer, D. E. Post, D. R. Mikkelsen, *et al.*, Computer Physics Communications **49**, 275 (1988).

[8] J. E. Kinsey, G.M. Staebler and R.E. Waltz, Phys. Plasmas **9**, 1676 (2002).

[9] G. Pereverzev and P. N. Yushmanov, Max-Planck Institut fur Plasmaphysik (IPP 5/98) (2002).

[10] G. Bateman, T. Onjun, and A. H. Krtiz, Plasma Phys. Control. Fusion **45**, 1939 (2003).

[11] T. Onjun, G. Bateman, A. H. Kritz, and G. Hammett, Phys. Plasmas **9**, 5018 (2002).

[12] G. W. Pacher, H. D. Pacher, A. S. Kukushkin, G. Janeschitz, and G. Pereversev, Nucl. Fusion **43**, 188 (2003).

[13] G. Cenacchi and A. Taroni, JET-IR(88) **03** (1988).

[14] M. Erba, A. Cherubini, V. V. Parail, and A. Taroni, Plasma Physics and Controlled Fusion **39**, 261 (1997).

[15] W. A. Houlberg, K. C. Shaing, S. P. Hirshman, and M. C. Zarnstorff, Phys. Plasmas **4**, 3231 (1997).

[16] A. B. Mikhailovskii, G. T. A. Huysmans, S. E. Sharapov, and W. Kerner, Plasma Phys. Rep **23**, 844 (1997).

[17] T. Onjun, A. H. Krtiz, G. Bateman, V. Parail, J. Lonnroth, and G. Huysmans, Phys. Plasmas **11**, 3006 (2004).

[18] T. Onjun, A. H. Krtiz, G. Bateman, V. Parail, H. Wilson, J. Lonnroth, G. Huysmans, and A. Dnestrovskij, Phys. Plasmas **11**, 1469 (2004).

[19] J. S. Lonnroth, V. V. Parail, G. Corrigan, *et al.*, Plasma Phys. Control. Fusion **45**, 1689 (2003).

[20] T. Onjun, A. H. Krtiz, G. Bateman, V. Parail, H. Wilson, and A. Dnestrovskij, Phys. Plasmas **12**, 012507 (2005).

[21] J.-S. Lonnroth, V. Parail, A. Dnestrovskij, C. Figarella, X. Garbet, H. Wilson, and J.-E. contributors, Plasma Physics and Controlled Fusion **46**, 1197 (2004).

[22] J.-S. Lonnroth, V. V. Parail, G. Corrigan, D. Heading, G. Huysmans, A. Loarte, *et al.*, Plasma Physics and Controlled Fusion **45**, 1689 (2003).

[23] H. R. Wilson, J. W. Connor, A. R. Field, S. J. Fielding, R. L. Miller, L. L. Lao, J. R. Ferron, and A. D. Turnbull, Phys. Plasmas **6**, 1925 (1999).

[24] P. Gohil, M. A. Mahdavi, L. Lao, *et al.*, Phys. Rev. Letters **61**, 1603 (1988).

[25] G. T. A. Huysmans *et al.*, in Proceeding of the 22nd EPS Conference on Controlled Fusion and Plasma Phys. Part I (1995).

[26] J. W. Connor, H. R. Hastie, H. R. Wilson, and R. L. Miller, Phys. Plasmas **5**, 2687 (1998).

[27] H. R. Wilson and R. L. Miller, Phys. Plasmas **6**, 873 (1999).

[28] J. Manickam, Phys. Fluids **B4** (1992).

[29] M. Sugihara, Y. Igitkhanov, G. Janeschitz, A. E. Hubbard, Y. Kamada, J. Lingertat, T. H. Osborne, and W. Suttrop, Nucl. Fusion **40**, 1743 (2000).

[30] T. H. Osborne, H. H. Burrell, R. J. Groebner, L. L. Lao, A. W. Leonard, R. Maingi, R. L. Miller, G. D. Porter, G. M. Staebler, and A. D. Turnbull, J. Nucl. Mater. **131**, 266-269 (1999).

[31] D. Hannum, G. Bateman, J. Kinsey, *et al.*, Phys. Plasmas **8**, 964 (2001).

[32] D. Boucher, J. Connor, W. Houlberg, M. Turner, *et al.*, Nucl. Fusion **40**, 1955 (2000).

[33] T. H. Osborne *et al.*, Plasma Physics and Controlled Fusion **42**, A 175 (2000).

[34] J. R. Ferron *et al.*, Phys. Plasmas **7**, 1976 (2002).

[35] L. L. Lao *et al.*, Nucl. Fusion **41**, 295 (2001).

[36] H. R. Wilson *et al.*, Proc. 28th EPS Conf. on Controlled Fusion and Plasma Physics (2001).

[37] H. Urano, Y. Kamada, H. Shirai, *et al.*, Plasma Phys. Control. Fusion **44**, 11 (2002).

[38] Y. Kamada, T. Hatae, T. Fukuda, *et al.*, Plasma Phys. Control. Fusion **41**, 1371 (1999).

[39] D. A. Mossessian *et al.*, Plasma Physics and Controlled Fusion **44**, 423 (2002).

[40] Y. Kamada, O. N. K. Ushigusa, *et al.*, Plasma Physics and Controlled Fusion **36**, A123 (1994).

[41] T. Hatae, Y. Kamada, S. Ishida, *et al.*, Plasma Physics and Controlled Fusion **40**, 1073 (1998).

[42] Y. Koide and the JT-60U Team, Phys. Plasmas **4**, 1623 (1997).

[43] Y. Kamada, R. Yoshida, K. Ushigusa, *et al.*, 16th IAEA Fusion Energy Conf. (1996).

[44] The JET Team (presented by J. G. Cordey), in *Proceedings of the Seventeenth International Atomic Energy Agency Fusion Energy Conference, (Yokahama, Japan, 19–24 October, 1998)* (International Atomic Energy Agency, Vienna, 1999), paper IAEA-F1-CN-69/EX7/1.

[45] J. Lingertat *et al.*, 24th EPS Conf. on Controlled Fusion and Plasma Physics, Berchtesgaden, 1977 .

*Table 1: Notation used in this paper.*

| Symbol | Units | Description |
|---|---|---|
| $a$ | m | Plasma minor radius (half-width) |
| $r$ | m | Flux surface minor radius (half-width) |
| $R$ | m | Major radius to geometric center of each flux surface |
| $\kappa$ | | Plasma elongation |
| $\delta$ | | Plasma triangularity |
| $B_T$ | Tesla | Vacuum toroidal magnetic field at R |
| $I_p$ | MA | Plasma current |
| $A_H$ | AMU | Hydrogenic isotope mass |
| $Z_{\text{eff}}$ | | Effective charge |
| $n_l$ | $10^{19}$ particles/m$^3$ | Line average density |
| $W_{\text{ped}}$ | MJ | Stored energy in pedestal region |
| $T_{\text{e,ped}}$ | keV | Electron temperature at the top of the pedestal |
| $n_{\text{e,ped}}$ | $10^{19}$ particles/m$^3$ | Electron density at the top of the pedestal |
| $\bar{n}_{20}$ | $10^{20}$ particles/m$^3$ | Line average electron density |
| $P_{\text{NBI}}$ | MW | NBI Heating power |
| $p$ | Pa | Plasma pressure |
| $q$ | | safety factor |
| $\rho$ | | Normalized minor radius |
| $\mu_0$ | H m$^{-1}$ | Permeability of free space |
| $\alpha$ | | normalized pressure gradient |
| $\alpha_c$ | | normalized critical pressure gradient of ballooning mode |

*Table 2: The basic parameters of ITER design.*

| Physical quantity | ITER |
|---|---|
| Major radius $R$ [m] | 6.2 |
| Minor radius $a$ [m] | 2.0 |
| Plasma current $I_p$ [MA] | 15.0 |
| Toroidal magnetic field $B_T$ [Tesla] | 5.3 |
| Elongation at the separatrix $\kappa_x$ | 1.85 |
| Triangularity at the separatrix $\delta_x$ | 0.48 |
| Average ion mass [AMU] | 2.5 |
| $\langle n_{e,20} \rangle$ | 1.0 |
| $n_{\mathrm{G},20}$ | 1.2 |
| $\langle n_e \rangle / n_{\mathrm{G}}$ | 0.8 |
| $P_{\mathrm{NBI}}$ [MW] | 33.0 |
| $P_{\mathrm{RF}}$ [MW] | 7.0 |
| $Z_{\mathrm{eff}}$ | 1.4 |

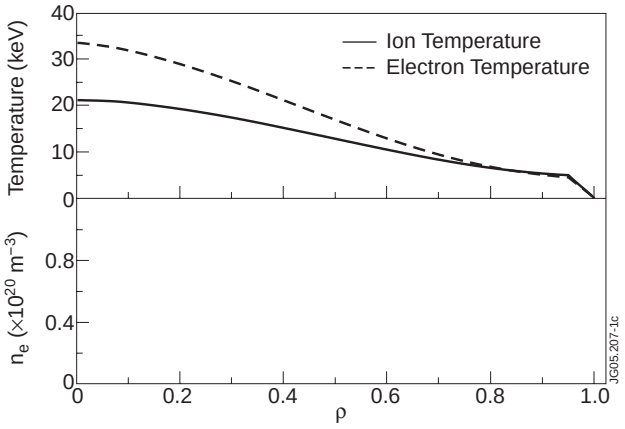


*Figure 1: Profiles for ion and electron temperature (top) and electron density (bottom) are shown as a function of normalized minor radius at a time just prior to an ELM crash. In the upper panel, the solid line shows the ion temperature and the dashed line shows the electron temperature.*

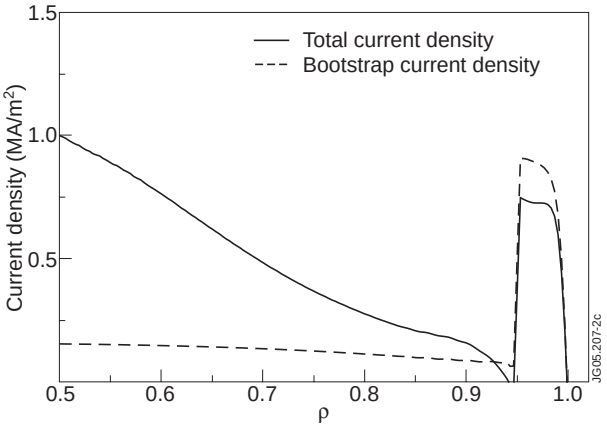


*Figure 2: Profiles for plasma current density and bootstrap current density are shown for the outer half of the plasma. These profiles are taken at the time just prior to an ELM crash. The solid line indicates the total plasma current density and the dashed line is the bootstrap current density.*

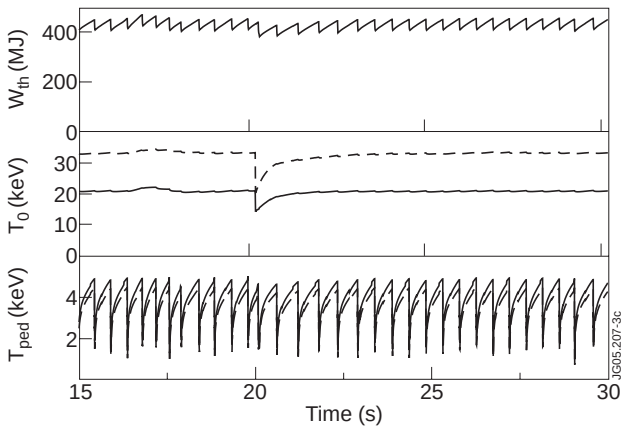


*Figure 3: The plasma stored energy (top panel), the central temperatures (middle panel), and the pedestal temperatures (bottom panel) are plotted as a function of time for the baseline ITER simulation. The electron temperatures are plotted as dashed lines while the ion temperatures are plotted as solid lines.*

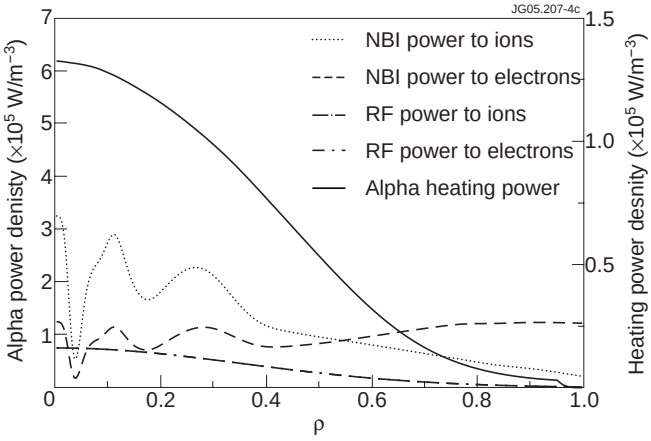


*Figure 4: The alpha heating power density profile is plotted with a solid line using the axis on the left while the NBI heating power density to the ions (dotted line) and electrons (dashed line) and the RF heating power density (chained lines) are plotted using the axis on the right. In this simulation, 40MW of auxiliary heating is used (33MW of NBI heating power and 7MW of RF heating power). The alpha heating power from the fusion reaction is about 133MW.*

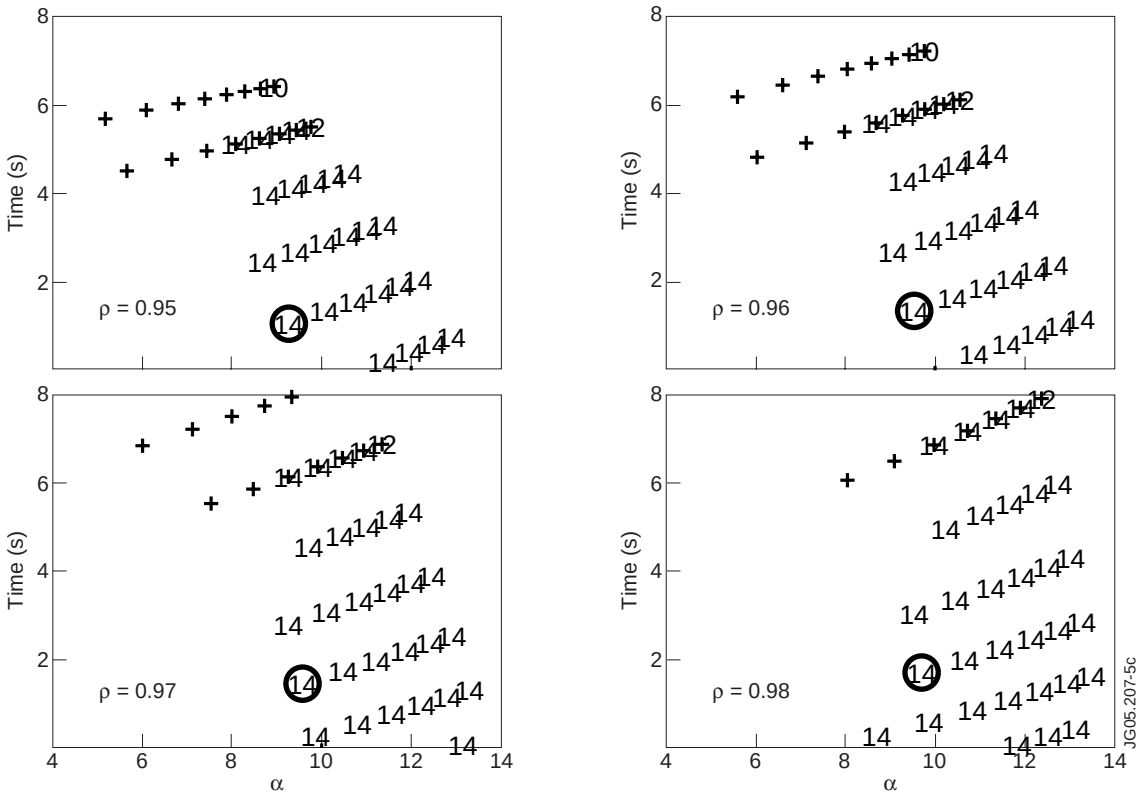


*Figure 5: Stability results obtained using the HELENA and MISHKA stability codes are plotted on an s-α stability diagram at four surfaces within the pedestal (ρ > 0.94) for the baseline ITER simulation. The region of instability associated with the infinite-n ideal ballooning modes is indicated with crosses. The numbers indicate the most unstable finite-n ballooning and low-n kink/peeling modes at each location on the s-α plane. Higher mode numbers (n≥10) correspond to finite-n ballooning modes. The region without numbers or crosses is the region where all modes are stable.*

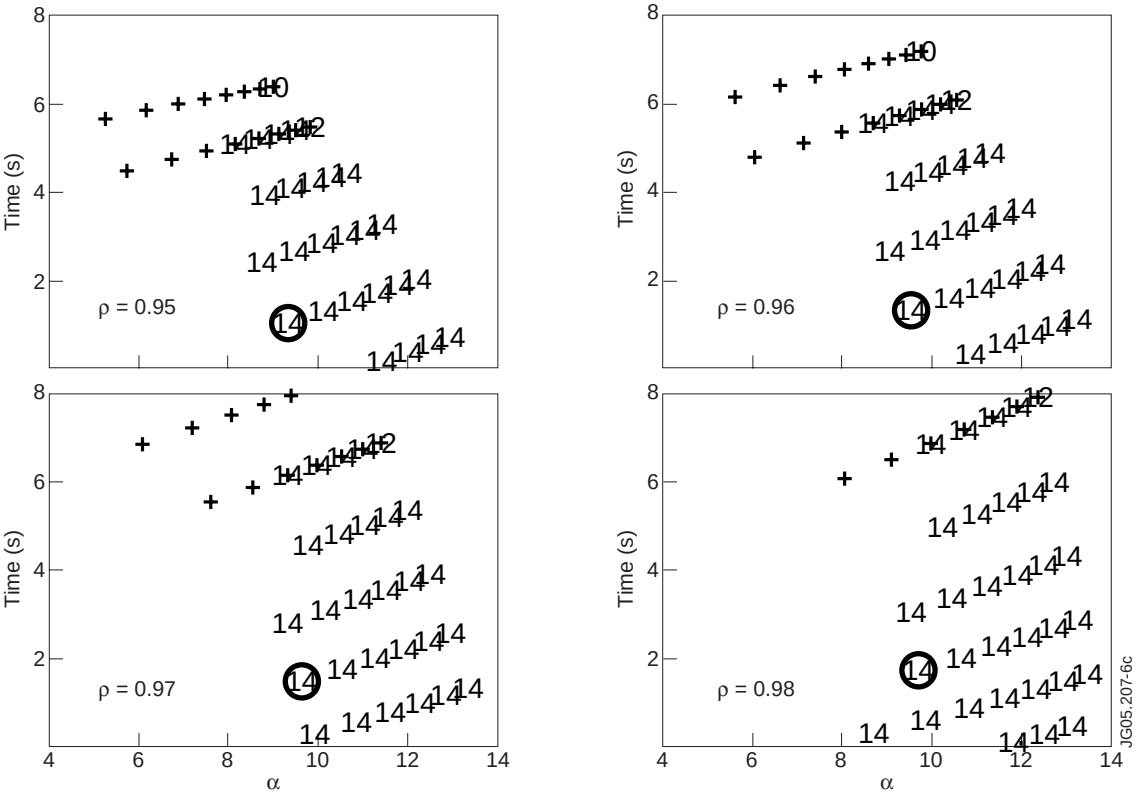


*Figure 6: The pedestal temperature (top panel) and fusion Q (bottom panel) are shown as a function of auxiliary heating power.*

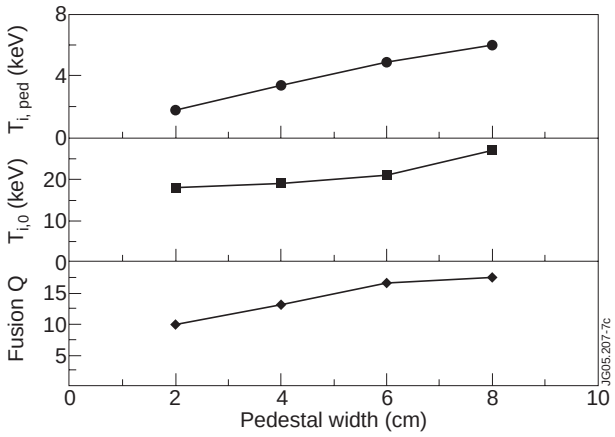


*Figure 7: The pedestal temperature and fusion Q are plotted as a function of pedestal width for JETTO simulations using the Mixed-Bohm/gyro-Bohm transport model (solid line) and corresponding BALDUR simulations using the Multi-Mode transport model (dashed line in bottom panel).*

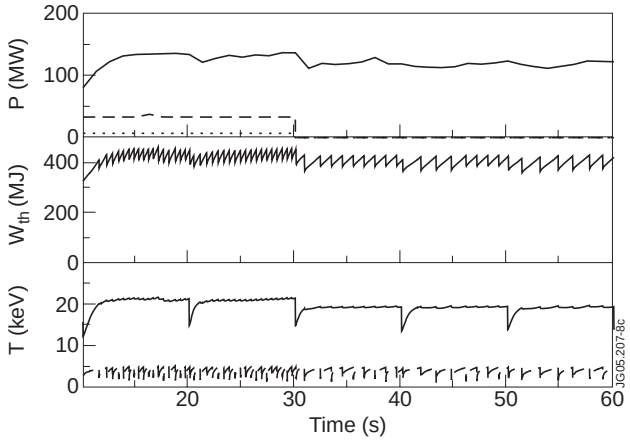


*Figure 8: In the top panel, the time history of the NBI heating (dashed line), RF heating (dotted line) and alpha power heating (solid line) is shown. The auxiliary heating was turned off at 30sec. In the middle panel, the time history of the stored energy is shown. In the bottom panel, the time history of the central temperature (solid line) and the pedestal temperature (dashed line) are shown. Both central and pedestal temperature decrease slightly after the auxiliary heating is turned off.*

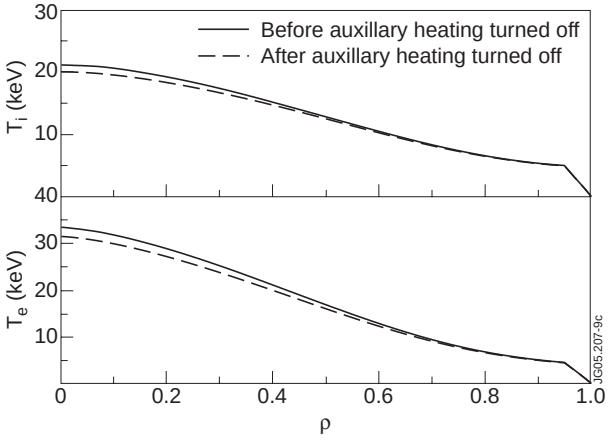


*Figure 9: Profiles for the ion and electron temperatures are shown at the time just prior to an ELM crash. The solid line is at a time when the auxiliary heating is on, while the dashed line is at a time after the auxiliary heating is turned off.*

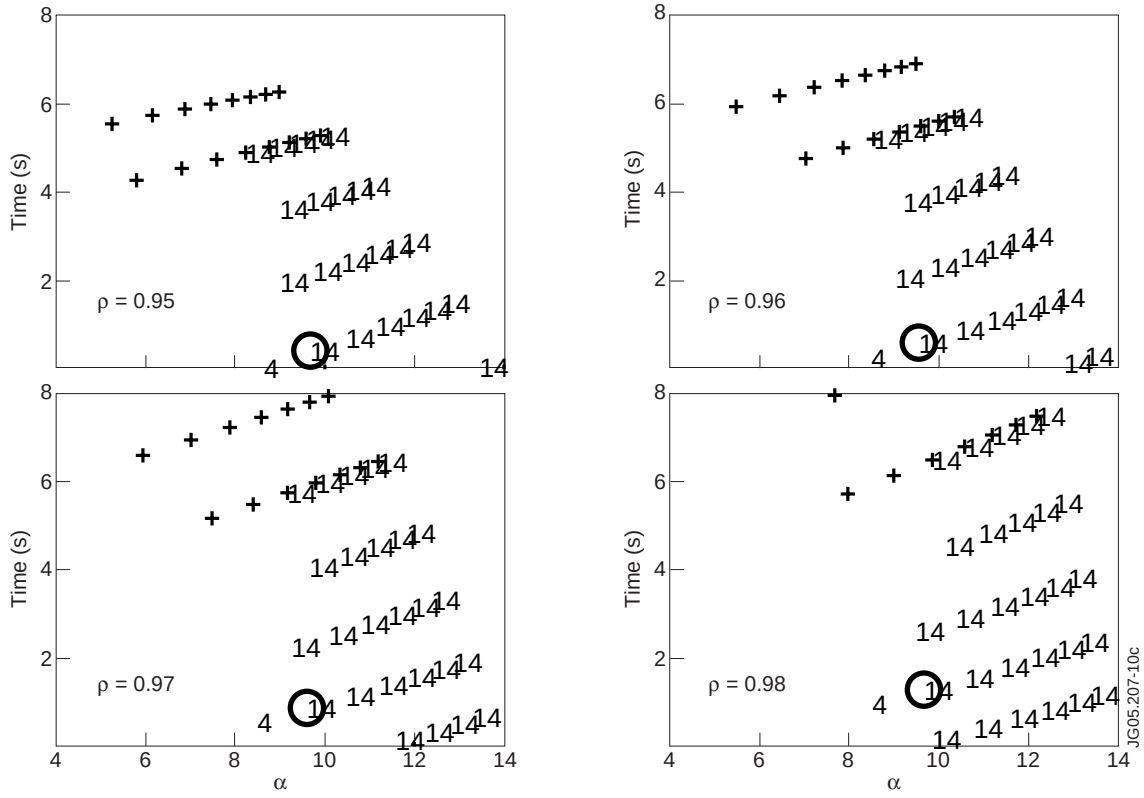


*Figure 10: Stability results obtained using the HELENA and MISHKA stability codes are plotted on an s-α stability diagram with flux surfaces ranging from ρ = 0.95 (top of the pedestal) to ρ = 0.98 for the ITER simulation after the auxiliary heating power is turned off. The region of instability associated with the infinite-n ideal ballooning modes is indicated with crosses. The numbers indicate the most unstable finite-n ballooning and low-n kink/peeling modes at each location on the s-α plane. Higher mode numbers (n≥10) correspond to finite-n ballooning modes. The region without numbers or crosses is the region where all modes are stable.*